Green Chemistry

PAPER

View Article Online
View Journal | View Issue

Cite this: *Green Chem.*, 2023, **25**, 7635

Stabilizing Cu^0–Cu^+ sites by Pb-doping for highly efficient CO_2 electroreduction to C_2 products†

Xiaodong Ma,[a,b] Xinning Song,[a,b] Libing Zhang,[a,b] Limin Wu,[a,b] Jiaqi Feng,[a,b] Shunhan Jia,[a,b] Xingxing Tan,[a,b] Liang Xu,[a,b] Xiaofu Sun *[a,b] and Buxing Han *[a,b,c]

Received 7th May 2023,
Accepted 14th August 2023

DOI: 10.1039/d3gc01506h

rsc.li/greenchem

The electrochemical CO_2 reduction reaction (CO_2RR) can convert CO_2 to C_2 hydrocarbons and oxygenate over Cu-based catalysts, and has great potential to store renewable energy and close the carbon cycle. Developing a facile method to modify the local electronic structure of Cu is a useful way to design efficient catalysts. Herein, we design a Pb-doping Cu_2O catalyst with controllable Cu^0–Cu^+ sites. The catalyst generated a high C_2 faradaic efficiency (FE) of 83.9% with a current density of 203.8 mA cm^{-2} at −1.1 V *vs.* RHE in a flow cell. *In situ* X-ray absorption spectroscopy and Raman spectroscopy revealed that the Pb doping in Cu_2O could stabilize the Cu^0–Cu^+ structure and enhance the CO adsorption and C–C coupling, leading to high activity for C_2 product formation. Theoretical calculations also show that Pb doping could reduce the energy barrier for both CO_2 activation and C–C coupling processes.

Introduction

The electrochemical CO_2 reduction reaction (CO_2RR) can convert CO_2 into valuable fuels or chemicals, which have great potential to mitigate the greenhouse effect, alleviate the energy crisis, and store intermittent electrical energy.[1–4] C_2 products including ethylene, ethanol, and acetic acid have higher energy density and economic value per unit mass compared with their C_1 counterparts.[5–9] Current research has paid increasing attention to the enhancement of conversion and selectivity for CO_2-to-C_2 products. Cu-based catalysts have been widely studied owing to their excellent performance in the electrochemical CO_2RR to C_{2+} products.[10–15] Previous studies show that the Cu^0–Cu^+ sites in Cu-based catalysts are the key active sites for producing the C_{2+} products, which are favorable for CO_2 activation and C–C coupling.[16–20] Therefore, it is of interest to modify the local electronic structure of Cu to achieve high activity and selectivity for CO_2-to-C_2 products.

Unfortunately, the surface Cu^+ is usually unstable, and it is prone to be reduced to Cu^0 at the high applied reducing potentials during the CO_2RR, leading to the loss of the performance of the CO_2RR to give C_2 products.[16, 21–25] Hence, it is extremely important to stabilize Cu^+ in the catalysts.[26,27] Some strategies such as surface modification,[17] electropolishing,[28] and doping[29] can stabilize the surface Cu^+ species. Among them, introducing a p-block metal dopant into Cu has been shown to be a promising strategy. It has been reported that the introduction of a p-block metal can effectively stabilize Cu^+ in Cu-based catalysts.[30–33] Not only that, some p-block metal elements such as In, Sn, Bi, and Pb have O affinity and can reduce the reaction energy barrier of the CO_2RR, as well as show high overpotentials for the H_2 evolution reaction (HER).[34–37] For example, Xie *et al.* screened Cu-based bimetallic catalysts for the CO_2RR to form C_{2+} products and found that Sn, In, Pb, and Bi in Cu-based bimetallic catalysts exhibited performances for inhibiting the HER.[35] Bai *et al.* used first-principles calculations to find that Sn doping into Cu-based catalysts can effectively suppress the HER without altering the activity toward CO_2 reduction, thereby improving the FE of ethanol.[36] Li *et al.* found that introducing Sn can enhance the surface oxophilicity of Cu–Sn alloy catalysts, which plays an important role in guiding the protonation of the key oxygenic intermediate and transforming CO_2 into ethanol.[34] Wang *et al.* developed Cu–Bi bimetallic aerogels as catalysts, which successfully improved the faradaic efficiency (FE) of ethylene in the CO_2RR.[37] Therefore, developing facile methods to construct p-block metal doped Cu catalysts with controllable Cu^0–Cu^+ sites is an effective way to realize the CO_2-to-C_2 products with high efficiency.

[a]*Beijing National Laboratory for Molecular Sciences, Key Laboratory of Colloid and Interface and Thermodynamics, Center for Carbon Neutral Chemistry, Institute of Chemistry, Chinese Academy of Sciences, Beijing 100190, P. R. China. E-mail: sunxiaofu@iccas.ac.cn, hanbx@iccas.ac.cn*

[b]*School of Chemical Sciences, University of Chinese Academy of Sciences, Beijing 100049, P. R. China*

[c]*Shanghai Key Laboratory of Green Chemistry and Chemical Processes, School of Chemistry and Molecular Engineering, East China Normal University, Shanghai 200062, P. R. China*

†Electronic supplementary information (ESI) available: Experimental procedures, Fig. S1–S16 and Table S1. See DOI: https://doi.org/10.1039/d3gc01506h

In this work, we have designed a Pb-doped Cu_2O electrocatalyst for highly efficient CO_2 reduction to C_2 products. It was discovered that the FE of C_2 products could reach 83.9% with good stability. Experimental and density functional theory (DFT) studies indicated that the doping of Pb in the catalyst can stabilize the Cu^0–Cu^+ structure, which could reduce the energy barrier of CO_2 activation and C–C coupling. As a result, it can improve the performance of the CO_2RR to form C_2 products.

Results and discussion

The detailed fabrication procedures of the electrocatalysts are discussed in the Methods section. In brief, as shown in Fig. 1A, 1 mmol of copper sulfate, 5 mL of ethanol, and 2 mL of oleic acid were added into 15 mL of deionized water and heated to 80 °C. Then, 5 mL of 1 M NaOH solution and 5 mL of 2 M glucose solution were added into the flask. The obtained reddish-brown precipitate was Cu_2O.[38] Subsequently, the Cu_2O powder was evenly dispersed in the lead acetate solution and stirred for a long time without light and air. The mass fraction of Pb doped into Cu_2O can be controlled with different stirring times. After stirring, we can obtain a series of Pb/Cu_2O-x catalysts, where x is the mass fraction of Pb in the catalysts measured by inductively coupled plasma optical emission spectroscopy (ICP-OES). The measured mass fraction of Pb was 1.2%, 2.1%, 3.4%, and 6.2%, respectively. Pb/Cu_2O-x was taken and uniformly loaded on a gas diffusion electrode (GDE) and electrochemically activated in a 3 M KOH aqueous solution. Finally, the e-Pb/Cu_2O-x GDE was obtained, where e stands for "after electrochemical activation".

The structure of e-Pb/Cu_2O-x was confirmed through powder X-ray diffraction (XRD) characterization, which showed the diffraction peaks of Cu, Cu_2O, and PbO (Fig. S1†). This result preliminarily indicated the co-existence of Cu^0 and Cu^+ in the catalysts. The scanning electron microscopy (SEM) and transmission electron microscopy (TEM) images of e-Pb/Cu_2O-3.4% are shown in Fig. 1B and C. We can see that e-Pb/Cu_2O-3.4% has a sheet-like morphology with an average diameter ranging from 400 to 600 nm. Other e-Pb/Cu_2O-x had similar morphological characteristics (Fig. S2†). The high-resolution TEM (HRTEM) images in Fig. 1D and Fig. S3† show that the spacings of the lattice fringe for all of the e-Pb/Cu_2O-x were 0.25 nm and 0.21 nm, which can be assigned to the (111) plane of Cu_2O and (111) plane of Cu, respectively.[39,40] Elemental distribution mappings illustrated a uniform distribution of Cu, O, and Pb over the entire architecture (Fig. 1E).

X-ray photoelectron spectroscopy (XPS) analysis was performed to study the composition and chemical nature of the

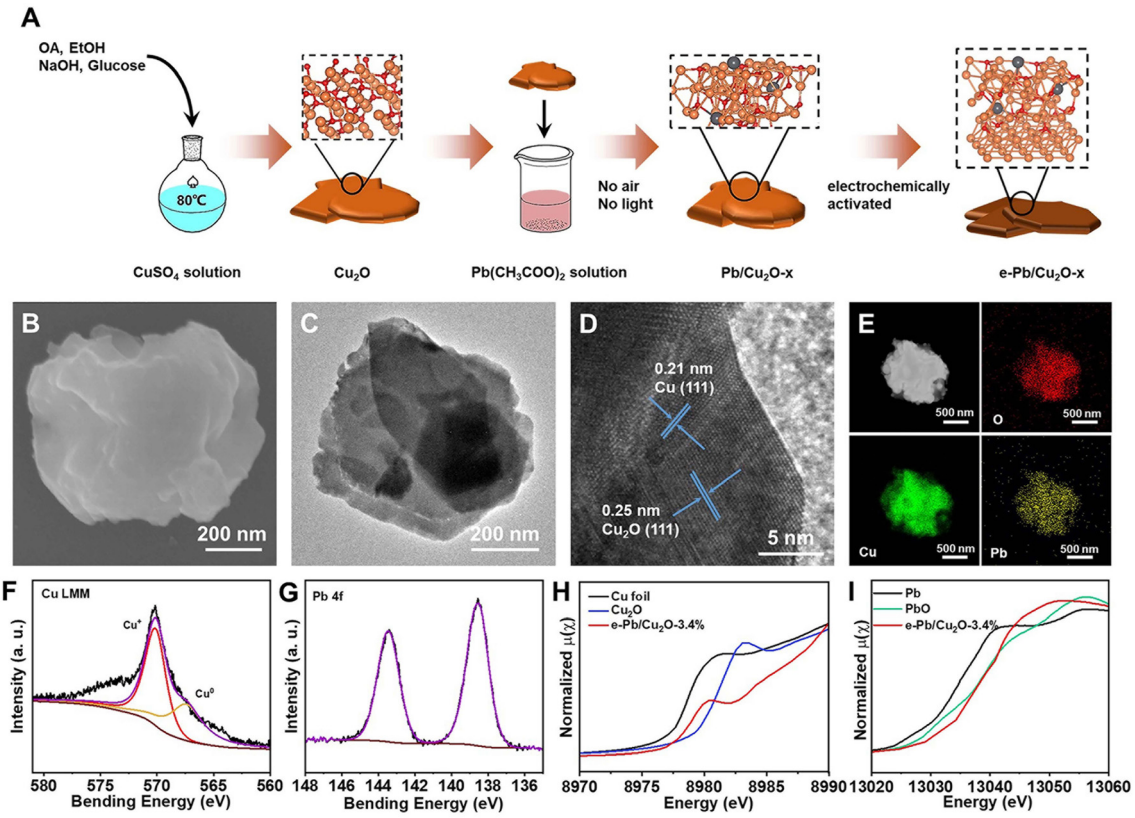

Fig. 1 (A) Schematic illustration of the preparation of e-Pb/Cu_2O-x. (B) SEM image of e-Pb/Cu_2O-3.4%. (C and D) TEM and HRTEM images of e-Pb/Cu_2O-3.4%. (E) Elemental mappings of e-Pb/Cu_2O-3.4%. (F) Cu LMM XPS spectra of e-Pb/Cu_2O-3.4%. (G) Pb 4f XPS spectra of e-Pb/Cu_2O-3.4%. (H) Cu K-edge XANES spectra of e-Pb/Cu_2O-3.4%. (I) Pb L-edge XANES spectra of e-Pb/Cu_2O-3.4%.

catalysts. The spectra of Cu 2p for e-Pb/Cu_2O-3.4% (Fig. S4†) displayed the fitting peaks, which were attributed to Cu^+ or Cu^0 (932.1 eV and 951.9 eV),[41,42] and the Auger LMM spectra of Cu further clarified two fitting peaks at 569.9 eV and 567.9 eV that belonged to Cu^+ and Cu^0 (Fig. 1F).[42,43] The spectra of Pb 4f (Fig. 1G) displayed the two fitting peaks of Pb at 138.5 and 143.2 eV, indicating that the valence of Pb in e-Pb/Cu_2O-3.4% was +2.[44] The same conclusions can be obtained from the XPS spectra of other e-Pb/Cu_2O-*x* samples (Fig. S5–S7†). Furthermore, X-ray absorption spectroscopy (XAS) was used to explore the detailed electronic structures of e-Pb/Cu_2O-3.4%. The X-ray absorption near-edge structure (XANES) spectra showed that the near-edge absorption energy (E_0) of Cu K-edge for e-Pb/Cu_2O-3.4% was between those of Cu and Cu_2O (Fig. 1H). It can be concluded that the average valence of Cu in e-Pb/Cu_2O-3.4% was between 0 and +1.[45–47] The coordination structures for Cu can be confirmed by the extended X-ray absorption fine structure (EXAFS) spectra (Fig. S8A and S9A†). The Cu–O coordination of Cu_2O and e-Pb/Cu_2O-3.4% were at the same peak (1.52 Å). The peak of the Cu–Cu coordination (2.61 Å) of e-Pb/Cu_2O-3.4% was between Cu and Cu_2O. These results further indicated the coexistence of Cu_2O and Cu structures in e-Pb/Cu_2O-3.4%.

Similarly, the E_0 of Pb L-edge was almost the same as that of PbO (Fig. 1I), demonstrating that the valence of Pb in e-Pb/Cu_2O-3.4% was +2.[48] The EXAFS spectra of Pb (Fig. S8B and S9B†) also showed that the Pb–O and Pb–Pb coordination was similar to those of PbO. These results are consistent with the data of XRD, XPS, and HRTEM.

The CO_2RR electrocatalytic activity of the as-prepared catalysts was carried out in a flow cell. In a typical experiment, the 3 M KOH aqueous solution was used as the electrolyte. ^{1}H nuclear magnetic resonance (NMR) spectroscopy and gas chromatography (GC) were adopted to determine and quantify the liquid and gas products from the CO_2RR. We can detect ethanol, acetate, formate, and trace methanol in liquid products, and H_2, CO, C_2H_4, and trace CH_4 in gas products. It can be found that the total FE of C_2 products with e-Pb/Cu_2O-*x* showed volcano-shaped dependence on the applied potentials (Fig. 2A). Significantly, e-Pb/Cu_2O-3.4% had the best activity with the highest C_2 product FE. The maximum C_2 product FE could reach 83.9% with a current density of 203.8 mA cm^{-2} at −1.1 V *vs.* RHE (Fig. 2B and C), which is comparable to those of many reported systems (Table S1†). The FEs of C_2H_4, ethanol, and acetate were 32.8%, 42.5%, and 8.6%, respectively. Different Pb contents in the catalysts can affect the CO_2-to-C_2 product performance obviously (Fig. S10†). The FE of C_2 products increased with the increase of Pb. However, when the mass fraction of Pb increased to 6.2%, the yield of CO increased, and the FE of the C_2 product was only 54.0%. In addition, different Pb contents in the catalysts can also affect the HER in the CO_2RR (Fig. S11†). The FE of H_2 was reduced until the Pb increased to 3.4%. Then the H_2 FE increased when the mass fraction of Pb increased to 6.2%. We then performed electrochemical impedance spectroscopy (EIS) to investigate the electrode/electrolyte interface properties. The

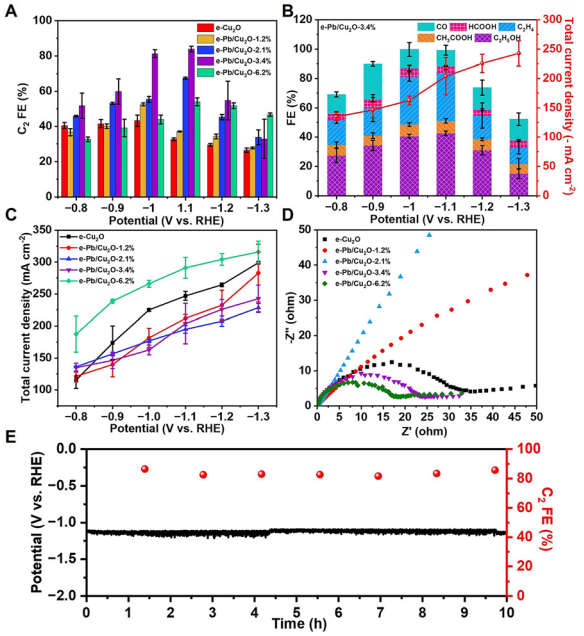

Fig. 2 (A) The FE for C_2 production over various catalysts at different applied potentials. (B) The FE of different products and total current density for e-Pb/Cu_2O-3.4% at different applied potentials. (C) The total current density for e-Cu_2O, e-Pb/Cu_2O-1.2%, e-Pb/Cu_2O-2.1%, e-Pb/Cu_2O-3.4% and e-Pb/Cu_2O-6.2% at different applied potentials. (D) Electrochemical impedance spectra for e-Cu_2O, e-Pb/Cu_2O-1.2%, e-Pb/Cu_2O-2.1%, e-Pb/Cu_2O-3.4%, and e-Pb/Cu_2O-6.2% at the open circuit potential (OCP) shown as a Nyquist plot. (E) Stability test for e-Pb/Cu_2O-3.4% at a constant current density of 200 mA cm^{-2}.

Nyquist plots were obtained by running the experiments at an open circuit potential (Fig. 2D). e-Pb/Cu_2O-3.4% had lower interfacial charge transfer resistance, which ensures a faster electron transfer during the reaction. These results indicated that appropriate Pb doping in e-Pb/Cu_2O-*x* could improve the C_2 product selectivity.

The stability of e-Pb/Cu_2O-3.4% in the flow cell system at a constant current density of 200 mA cm^{-2} is shown in Fig. 2E. There was no obvious decay in the potential and FE of C_2 products during the 10 h test. e-Pb/Cu_2O-3.4% after the reaction, denoted as e-Pb/Cu_2O-3.4%-R, was examined by TEM and XRD. The morphology and structure of the catalysts did not change notably, further indicating its excellent stability (Fig. S12 and S13†). The fine structure was analyzed by XAS (Fig. S14†). The valence and structure of Cu and Pb in e-Pb/Cu_2O-3.4%-R were almost the same as those in e-Pb/Cu_2O-3.4%. These results suggest that the structure of the catalyst can remain stable during the CO_2RR.

To explore the behavior of e-Pb/Cu_2O-3.4% in the CO_2RR, we carried out detailed experimental analysis. *In situ* XAS was first performed to monitor the valence change and coordination environment of Cu under different potentials. In Fig. 3A, the Cu K-edge E_0 of e-Pb/Cu_2O-3.4% reflects the change in the oxidation state. Compared with the data of the Cu K-edge E_0 of Cu foil and Cu_2O, we can determine the valence of Cu in e-Pb/Cu_2O-3.4% at each applied potential

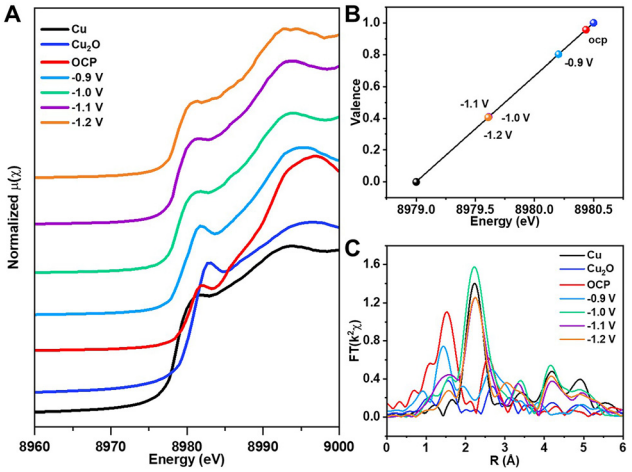

Fig. 3 (A) *In situ* XANES spectra at Cu K-edge for e-Pb/Cu_2O-3.4% at different applied potentials. (B) The average oxidation state of Cu in e-Pb/Cu_2O-3.4% at different applied potentials from Cu K-edge XANES. (C) R spatial data of Cu K-edge EXAFS spectra for e-Pb/Cu_2O-3.4% at different applied potentials.

(Fig. 3B). It can be seen that the average valence of Cu in e-Pb/Cu_2O-3.4% decreased from +0.95 at OCP to +0.8 at −0.9 V *vs.* RHE, and finally it would be stable around +0.4 under a higher potential. This indicated that the local electronic structure of Cu with positive valence sites could be retained during the CO_2RR.[45–47] From the EXAFS spectra in Fig. 3C, it can be seen that the Cu–Cu and Cu–O coordination is close to those in Cu_2O at −0.9 V *vs.* RHE, suggesting that e-Pb/Cu_2O-3.4% could still maintain the Cu_2O structure, but a small amount of Cu^0 appeared. When the applied potential increased to a value higher than −1.0 V *vs.* RHE, the Cu–Cu coordination of e-Pb/Cu_2O-3.4% was close to that of Cu foil, and the Cu–O coordination of e-Pb/Cu_2O-3.4% was close to that of Cu_2O. The complete Cu_2O structure could not be maintained in the catalysts, and a part of Cu^+ was reduced to Cu^0. These results prove that the Cu^0–Cu^+ structure exists in e-Pb/Cu_2O-3.4% during the electrochemical CO_2RR.

In situ Raman spectroscopy measurements were conducted to identify the possible intermediates. As shown in Fig. 4A, the Raman peaks around 2060 cm^{-1}, 1556 cm^{-1}, and 1436 cm^{-1} can be attributed to *CO, $*COO^-$, and $*HCOO^-$, respectively.[15,49–53] These important reaction intermediates were adsorbed on the surface of e-Pb/Cu_2O-3.4% during the CO_2RR, which could promote the occurrence of C–C coupling and increase the FE of C_2 products. The peak at 603 cm^{-1} was attributed to the Cu_2O structure.[50,53,54] However, it would disappear when the applied potential was higher than −1.1 V *vs.* RHE. Moreover, the new characteristic peak appeared at 525 cm^{-1}, which can be attributed to CuO_x.[50,53,54] It suggested the existence of the Cu^0–Cu^+ structure in the catalysts. The signal of Cu–CO was also detected at 361 cm^{-1}, indicating that the generated CO was adsorbed on the catalyst.

For comparison, we also obtained the *in situ* Raman spectra over e-Cu_2O (Fig. 4B). At a potential of −1.1 V *vs.* RHE, we cannot observe the CuO_x characteristic peak at 525 cm^{-1}, indicating that Cu_2O was reduced to Cu during the reaction.[55] Compared with the Cu^0–Cu^+ structure, Cu^0 had a poor performance for C–C coupling. Therefore, the doping of Pb in the catalyst could stabilize the Cu^0–Cu^+ structure and improve the catalytic performance for CO_2-to-C_2 products.

According to Raman data, CO is an important intermediate in CO_2-to-C_2 products. The increase of CO adsorption on the catalysts can increase the C_2 product FE. The detailed experimental procedures of the gas electroresponse experiments are discussed in the Methods section. The gas electroresponse experiments clearly showed the capacity for the adsorption of CO on e-Pb/Cu_2O-*x* and e-Cu_2O (Fig. 4C).[56] Compared with other materials, e-Pb/Cu_2O-3.4% showed the best capacity of adsorbing CO. This indicated that moderate Pb doping can improve the adsorption of a *CO intermediate, leading to high catalytic performance for C_2 product formation.

To better understand the reaction mechanism, we performed correlative theoretical calculations through DFT. All the simulated data and detailed procedures are shown in the ESI.† Based on the materials characterization, we have established the structural model of e-Pb/Cu_2O-3.4%. For e-Pb/Cu_2O-3.4%, a Cu(111) and Cu_2O(111) facet heterostructure was used as a model and a part of Cu in Cu_2O was replaced with Pb (Fig. S15†). We named it Cu(111)–Cu_2O(111)–Pb. Previous studies showed that the adsorption of *CO on Cu^+ is stronger

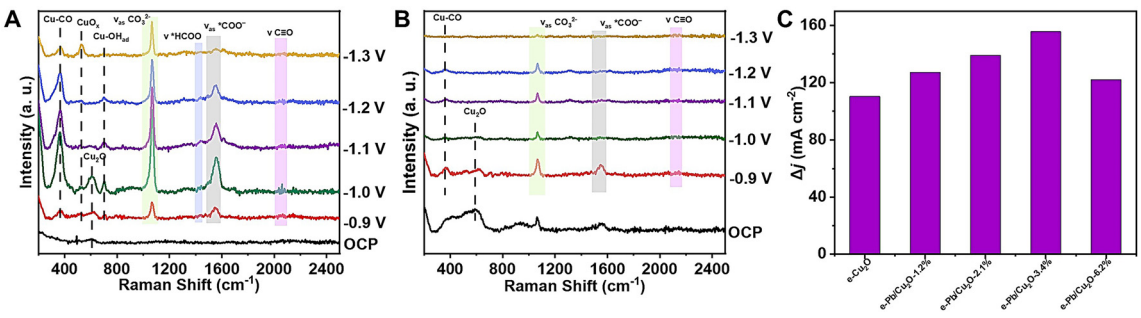

Fig. 4 (A) *In situ* Raman spectra at different applied potentials for e-Pb/Cu_2O-3.4%. (B) *In situ* Raman spectra at different applied potentials for e-Cu_2O. (C) The results of CO adsorption responses for the catalysts.

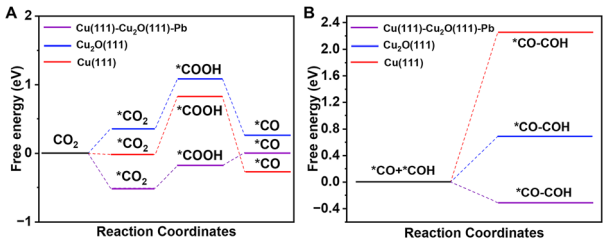

Fig. 5 (A) Gibbs free-energy diagrams for CO_2 activation on different simulated models. (B) Gibbs free-energy diagrams for C–C coupling on different simulated models.

than that on Cu^0.[28,57] The $Cu_2O(111)$ facet and Cu(111) were used to compare with Cu(111)–$Cu_2O(111)$–Pb to explore the effect of Pb doping.

The catalytic pathway of CO_2 activation is illustrated in Fig. 5A. It can be seen that the formation of *COOH from $*CO_2$ on the three models was highly endergonic and acted as the rate-determining step. The Gibbs free energy for $*CO_2$ to *COOH on Cu(111)–$Cu_2O(111)$–Pb was only about 0.33 eV, which was much lower than that on $Cu_2O(111)$ (0.73 eV) and Cu(111) (0.85 eV). This indicated that the doping of Pb greatly reduced the reaction energy barrier of $*CO_2$ to *COOH, which contributed to easier CO_2 activation. The C–C coupling process was studied subsequently (Fig. 5B). We have compared different coupling pathways (*CO–*CO, *CO–*COH, *CO–*CHO, and *CHO–*CHO) and found that the *CO–*COH coupling had a lower Gibbs free energy. The Gibbs free energy of this coupling process on Cu(111)–$Cu_2O(111)$–Pb was −0.31 eV, while it would be highly endergonic on $Cu_2O(111)$ (0.69 eV) and Cu(111) (2.26 eV).

Therefore, by combining the above simulation data, it is found that Pb doping can be beneficial not only for the activation of CO_2 but also the improvement of the C–C coupling, leading to the enhancement of the CO_2RR to form C_2 products.

Conclusions

In summary, a series of Pb-doped Cu_2O catalysts have been successfully designed and synthesized for the efficient electrochemical CO_2RR to form C_2 products. e-Pb/Cu_2O-3.4% exhibited the highest performance with a C_2 product FE of 83.9% in the flow cell. The catalyst also showed good stability in 10 h. *In situ* characterization revealed that Pb doping could stabilize the Cu^0–Cu^+ structure in e-Pb/Cu_2O-3.4% during the electrochemical CO_2RR, which had strong adsorption ability for the *CO intermediate. DFT calculations suggested that the doping of Pb could reduce the reaction energy barrier of $*CO_2$ to *COOH and C–C coupling processes simultaneously. This work provides a facile strategy for the design of Cu-based catalysts to improve the production of C_2 products from the CO_2RR. We believe that it may inspire new exploration of electrocatalyst design in the future.

Author contributions

X.D.M., X.F.S., and B.X.H. proposed the project, designed the experiments, and wrote the manuscript; M.X.D. performed the whole experiments; X.N.S., L.B.Z., L.M.W., J.Q.F., S.H.J., X.X.T., and L.X. performed the analysis of experimental data; X.F.S. and B.X.H. supervised the whole project.

Data availability

All experimental data are available in the ESI.†

Conflicts of interest

The authors declare no competing financial interests.

Acknowledgements

The work was supported by the National Key Research and Development Program of China (2020YFA0710203), National Natural Science Foundation of China (22002172, 22203099, 21890761, and 22121002), Beijing Natural Science Foundation (J210020), China Postdoctoral Science Foundation (2022M713200), and Photon Science Center for Carbon Neutrality. The X-ray absorption spectroscopy measurements were performed at Beamline 1W1B and 4B9A at Beijing Synchrotron Radiation Facility (BSRF).

References

1 I. Sullivan, A. Goryachev, I. A. Digdaya, X. Li, H. Atwater, D. A. Vermaas and C. Xiang, *Nat. Catal.*, 2021, **4**, 952–958.
2 Y. Zhai, P. Han, Q. Yun, Y. Ge, X. Zhang, Y. Chen and H. Zhang, *eScience*, 2022, **2**, 467–485.
3 L. Zhang, J. Feng, S. Liu, X. Tan, L. Wu, S. Jia, L. Xu, X. Ma, X. Song, J. Ma, X. Sun and B. Han, *Adv. Mater.*, 2023, **35**, 2209590.
4 X. Sun, Q. Zhu, X. Kang, H. Liu, Q. Qian, Z. Zhang and B. Han, *Angew. Chem., Int. Ed.*, 2016, **55**, 6771–6775.
5 P. Li, J. Bi, J. Liu, Y. Wang, X. Kang, X. Sun, J. Zhang, Z. Liu, Q. Zhu and B. Han, *J. Am. Chem. Soc.*, 2023, **145**, 4675–4682.
6 W. Nie, G. P. Heim, N. B. Watkins, T. Agapie and J. C. Peters, *Angew. Chem., Int. Ed.*, 2023, **62**, e202216102.
7 D. Wang, J. Mao, C. Zhang, J. Zhang, J. Li, Y. Zhang and Y. Zhu, *eScience*, 2023, **3**, 100119.
8 R. De, S. Gonglach, S. Paul, M. Haas, S. S. Sreejith, P. Gerschel, U. P. Apfel, T. H. Vuong, J. Rabeah, S. Roy and W. Schofberger, *Angew. Chem., Int. Ed.*, 2020, **59**, 10527–10534.
9 Y. Zheng, A. Vasileff, X. Zhou, Y. Jiao, M. Jaroniec and S. Qiao, *J. Am. Chem. Soc.*, 2019, **141**, 7646–7659.

10 L. Xu, X. Ma, L. Wu, X. Tan, X. Song, Q. Zhu, C. Chen, Q. Qian, Z. Liu, X. Sun, S. Liu and B. Han, *Angew. Chem., Int. Ed.*, 2022, **61**, e202210375.
11 Y. Yang, S. Louisia, S. Yu, J. Jin, I. Roh, C. Chen, M. V. F. Guzman, J. Feijoo, P. C. Chen, H. Wang, C. J. Pollock, X. Huang, Y. T. Shao, C. Wang, D. A. Muller, H. D. Abruna and P. Yang, *Nature*, 2023, **614**, 262–269.
12 Z. Gu, H. Shen, Z. Chen, Y. Yang, C. Yang, Y. Ji, Y. Wang, C. Zhu, J. Liu, J. Li, T.-K. Sham, X. Xu and G. Zheng, *Joule*, 2021, **5**, 429–440.
13 Y. Liang, J. Zhao, Y. Yang, S. Hung, J. Li, S. Zhang, Y. Zhao, A. Zhang, C. Wang, D. Appadoo, L. Zhang, Z. Geng, F. Li and J. Zeng, *Nat. Commun.*, 2023, **14**, 474.
14 Y. Yang, A. He, H. Li, Q. Zou, Z. Liu, C. Tao and J. Du, *ACS Catal.*, 2022, **12**, 12942–12953.
15 X. Yan, C. Chen, Y. Wu, Y. Chen, J. Zhang, R. Feng, J. Zhang and B. Han, *Green Chem.*, 2022, **24**, 1989–1994.
16 X. Yuan, S. Chen, D. Cheng, L. Li, W. Zhu, D. Zhong, Z. J. Zhao, J. Li, T. Wang and J. Gong, *Angew. Chem., Int. Ed.*, 2021, **60**, 15344–15347.
17 C. Lim, M. Yilmaz, J. M. Arce-Ramos, A. D. Handoko, W. J. Teh, Y. Zheng, Z. Khoo, M. Lin, M. Isaacs, T. Tam, Y. Bai, C. K. Ng, B. S. Yeo, G. Sankar, I. Parkin, K. Hippalgaonkar, M. Sullivan, J. Zhang and Y. Lim, *Nat. Commun.*, 2023, **14**, 335.
18 M. Li, Y. Ma, J. Chen, R. Lawrence, W. Luo, M. Sacchi, W. Jiang and J. Yang, *Angew. Chem., Int. Ed.*, 2021, **60**, 11487–11493.
19 P. M. Krzywda, A. P. Rodríguez, N. E. Benes, B. T. Mei and G. Mul, *Appl. Catal., B*, 2022, **316**, 121512.
20 C. Liu, X. Zhang, J. Huang, M. Guan, M. Xu and Z. Gu, *ACS Catal.*, 2022, **12**, 15230–15240.
21 S. Nitopi, E. Bertheussen, S. B. Scott, X. Liu, A. K. Engstfeld, S. Horch, B. Seger, I. E. L. Stephens, K. Chan, C. Hahn, J. K. Norskov, T. F. Jaramillo and I. Chorkendorff, *Chem. Rev.*, 2019, **119**, 7610–7672.
22 H. Li, T. Liu, P. Wei, L. Lin, D. Gao, G. Wang and X. Bao, *Angew. Chem., Int. Ed.*, 2021, **60**, 14329–14333.
23 J. Sang, P. Wei, T. Liu, H. Lv, X. Ni, D. Gao, J. Zhang, H. Li, Y. Zang, F. Yang, Z. Liu, G. Wang and X. Bao, *Angew. Chem., Int. Ed.*, 2022, **61**, e202114238.
24 Y. Zang, T. Liu, P. Wei, H. Li, Q. Wang, G. Wang and X. Bao, *Angew. Chem., Int. Ed.*, 2022, **61**, e202209629.
25 J. Feng, L. Wu, S. Liu, L. Xu, X. Song, L. Zhang, Q. Zhu, X. Kang, X. Sun and B. Han, *J. Am. Chem. Soc.*, 2023, **145**, 9857–9866.
26 J. Liu, L. Cheng, Y. Wang, R. Chen, C. Xiao, X. Zhou, Y. Zhu, Y. Li and C. Li, *J. Mater. Chem. A*, 2022, **10**, 8459–8465.
27 S. Mu, H. Lu, Q. Wu, L. Li, R. Zhao, C. Long and C. Cui, *Nat. Commun.*, 2022, **13**, 3694.
28 P. De Luna, R. Quintero-Bermudez, C.-T. Dinh, M. B. Ross, O. S. Bushuyev, P. Todorović, T. Regier, S. O. Kelley, P. Yang and E. H. Sargent, *Nat. Catal.*, 2018, **1**, 103–110.
29 W. Ma, S. Xie, T. Liu, Q. Fan, J. Ye, F. Sun, Z. Jiang, Q. Zhang, J. Cheng and Y. Wang, *Nat. Catal.*, 2020, **3**, 478–487.
30 Y. Wang, L. Cheng, Y. Zhu, J. Liu, C Xiao, R. Chen, L. Zhang, Y. Li and C. Li, *Appl. Catal., B*, 2022, **317**, 121650.
31 R. Imania, Z. Qiu, R. Younesi, M. Pazokib, D. Fernandes, P. Mitev, T. Edvinsson and H. Tian, *Nano Energy*, 2018, **49**, 40–50.
32 W. Zhang, P. He, C. Wang, T. Ding, T Chen, X. Liu, L Cao, T. Huang, X. Shen, O. Usoltsev, A. Bugaev, Y. Lin and T. Yao, *J. Mater. Chem. A*, 2020, **8**, 25970.
33 W. Guo, S. Liu, X. Tan, R. Wu, X. Yan, C. Chen, Q. Zhu, L. Zheng, J. Ma, J. Zhang, Y. Huang, X. Sun and B. Han, *Angew. Chem., Int. Ed.*, 2021, **60**, 21979–21987.
34 M. Li, N. Song, W. Luo, J. Chen, W. Jiang and J. Yang, *Adv. Sci.*, 2023, **10**, 2204579.
35 M. Xie, Y. Shen, W. Ma, D. Wei, B. Zhang, Z. Wang, Y. Wang, Q. Zhang, S. Xie, C. Wang and Y. Wang, *Angew. Chem., Int. Ed.*, 2022, **61**, e202213423.
36 X. Bai, L. Shi, Q. Li, C. Ling, Y. Ouyang, S. Wang and J. Wang, *Energy Environ. Mater.*, 2022, **5**, 892–898.
37 Y. Wang, L. Cheng, Y. Zhu, J. Liu, C. Xiao, R. Chen, L. Zhang, Y. Li and C. Li, *Appl. Catal., B*, 2022, **317**, 121650.
38 C. Zhan, Q. Wang, L. Zhou, X. Han, Y. Wanyan, J. Chen, Y. Zheng, Y. Wang, G. Fu, Z. Xie and Z. Tian, *J. Am. Chem. Soc.*, 2020, **142**, 14134–14141.
39 P. Wang, H. Yang, Y. Xu, X. Huang, J. Wang, M. Zhong, T. Cheng and Q. Shao, *ACS Nano*, 2021, **15**, 1039–1047.
40 Y. Jiang, T. Xia, L. Shen, J. Ma, H. Ma, T. Sun, F. Lv and N. Zhu, *ACS Catal.*, 2021, **11**, 2949–2955.
41 X. Ma, L. Xu, S. Liu, L. Zhang, X. Tan, L. Wu, J. Feng, Z. Liu, X. Sun and B. Han, *Chem. Catal.*, 2022, **2**, 3207–3224.
42 S. Lee, H. Jung, N. Kim, H. Oh, B. Min and Y. Hwang, *J. Am. Chem. Soc.*, 2018, **140**, 8681–8689.
43 X. Chang, T. Wang, Z. Zhao, P. Yang, J. Greeley, R. Mu, G. Zhang, Z. Gong, Z. Luo, J. Chen, Y. Cui, G. Ozin and J. Gong, *Angew. Chem., Int. Ed.*, 2018, **57**, 15415–15419.
44 T. Ng, C. Chan, M. Lo, Z. Guan and C. Lee, *J. Mater. Chem. A*, 2015, **3**, 9081–9085.
45 S. F. Hung, A. Xu, X. Wang, F. Li, S. H. Hsu, Y. Li, J. Wicks, E. G. Cervantes, A. S. Rasouli, Y. C. Li, M. Luo, D. H. Nam, N. Wang, T. Peng, Y. Yan, G. Lee and E. H. Sargent, *Nat. Commun.*, 2022, **13**, 819.
46 X. Wang, P. Ou, A. Ozden, S.-F. Hung, J. Tam, C. M. Gabardo, J. Y. Howe, J. Sisler, K. Bertens, F. P. G. de Arquer, R. K. Miao, C. P. O'Brien, Z. Wang, J. Abed, A. S. Rasouli, M. Sun, A. H. Ip, D. Sinton and E. H. Sargent, *Nat. Energy*, 2022, **7**, 170–176.
47 J. Li, A. Ozden, M. Wan, Y. Hu, F. Li, Y. Wang, R. R. Zamani, D. Ren, Z. Wang, Y. Xu, D. H. Nam, J. Wicks, B. Chen, X. Wang, M. Luo, M. Graetzel, F. Che, E. H. Sargent and D. Sinton, *Nat. Commun.*, 2021, **12**, 2808.
48 C. Li, Z. Li, J. Wang, W. Xiong, H. Yan, Y. Bai, D. O'Hare and Y. Zhao, *Chem. Eng. J.*, 2023, **462**, 141926.
49 G. Shi, Y. Xie, L. Du, X. Fu, X. Chen, W. Xie, T. Lu, M. Yuan and M. Wang, *Angew. Chem., Int. Ed.*, 2022, **61**, e202203569.
50 H. Li, P. Wei, D. Gao and G. Wang, *Curr. Opin. Green Sustainable Chem.*, 2022, **34**, 100589.

51 Z. Z. Niu, F. Y. Gao, X. L. Zhang, P. P. Yang, R. Liu, L. P. Chi, Z. Z. Wu, S. Qin, X. Yu and M. R. Gao, *J. Am. Chem. Soc.*, 2021, **143**, 8011–8021.
52 Z. Pan, K. Wang, K. Ye, Y. Wang, H.-Y. Su, B. Hu, J. Xiao, T. Yu, Y. Wang and S. Song, *ACS Catal.*, 2020, **10**, 3871–3880.
53 X. Chen, D. A. Henckel, U. O. Nwabara, Y. Li, A. I. Frenkel, T. T. Fister, P. J. A. Kenis and A. A. Gewirth, *ACS Catal.*, 2019, **10**, 672–682.
54 Y. Zhao, X. Zu, R. Chen, X. Li, Y. Jiang, Z. Wang, S. Wang, Y. Wu, Y. Sun and Y. Xie, *J. Am. Chem. Soc.*, 2022, **144**, 10446–10454.
55 M. F. Saleem, Y. A. Haleem, W. Sun, L. Ma and D. Wang, *J. Raman Spectrosc.*, 2020, **51**, 1286–1294.
56 B. Yang, K. Liu, H. Li, C. Liu, J. Fu, H. Li, J. E. Huang, P. Ou, T. Alkayyali, C. Cai, Y. Duan, H. Liu, P. An, N. Zhang, W. Li, X. Qiu, C. Jia, J. Hu, L. Chai, Z. Lin, Y. Gao, M. Miyauchi, E. Cortes, S. A. Maier and M. Liu, *J. Am. Chem. Soc.*, 2022, **144**, 3039–3049.
57 Y. Zhou, F. Che, M. Liu, C. Zou, Z. Liang, P. De Luna, H. Yuan, J. Li, Z. Wang, H. Xie, H. Li, P. Chen, E. Bladt, R. Quintero-Bermudez, T. Sham, S. Bals, J. Hofkens, D. Sinton, G. Chen and E. Sargent, *Nat. Chem.*, 2018, **10**, 974–980.